Electronic Supplementary Material (ESI) for JAAS.

Supplementary Information: "ANN-LIBS Analysis of Mixture Plasmas: Detection of Xenon"

Homa Saeidfirozeh*[a ‡], Ashwin Kumar Myakalwar[b‡], Petr Kubelík[ac‡], Amirhossein Ghaderi[d], Vojta Laitl[a,e], Lukáš Petera[a], Paul B. Rimmer[f], Oliver Shorttle[g,h], Alan N. Heays[a], Anna Křivková[a,i], Miroslav Krus[j], Svatopluk Civiš[a], Jorge Yáñez*[b], Erik Képeš[k,l], Pavel Pořízka[k,l], and Martin Ferus[a]

[a] J. Heyrovský Institute of Physical Chemistry, Czech Academy of Sciences, Dolejškova 3, CZ 18223 Prague 8, Czech Republic.
[b] Laboratorio de Trazas elementales y Especiación, Facultad de Ciencias Químicas, Universidad de Concepción, Concepción, Chile.
[c] Department of Radiation and Chemical Physics, Institute of Physics, Academy of Sciences of the Czech Republic, Na Slovance 1999/2, CZ18221 Prague 8, Czech Republic.
[d] Centre for Vision Research, 4700 Keele St, ON M3J 1P3, York U, Toronto, ON, Canada.
[e] University of Chemistry and Technology Prague, Faculty of Chemical Engineering B, Technická 5, CZ16628 Prague 6 Dejvice, Czech Republic.
[f] Cavendish Astrophysics, University of Cambridge, JJ Thomson Ave, Cambridge, CB3 OHE.
[g] Institute of Astronomy, University of Cambridge, CB3 0HA, UK.
[h] Department of Earth Sciences, University of Cambridge, CB2 3EQ, UK.
[i] Czech Technical University in Prague, Faculty of Nuclear Sciences and Physical Engineering, Brˇehová 78/7, 11519 Prague 1, Czech Republic.
[j] Institute of Plasma Physics, Czech Academy of Sciences, Za Slovankou 1782/3, 182 00 Prague 8, Czech Republic.
[k] Central European Institute of Technology, Brno University of Technology, Purkynˇova 656/123, CZ-61200, Brno, Czech Republic.
[l] Brno University of Technology, Faculty of Mechanical Engineering, Institute of Physical Engineering, Technická 2, CZ-61669, Brno, Czech Republic.
‡ These authors contributed equally to this work.
∗ Corresponding authors: jyanez@udec.cl, homa.saeidfirouzeh@jh-inst.cas.cz

ABSTRACT

Here we provide supplementary information of the article "ANN-LIBS Analysis of Mixture Plasmas: Detection of Xenon". The sections outlined are named accordingly to main text and comprise supporting information to key concepts presented therein.

Theory and Computation

In a classical LIBS protocol, the Boltzmann distribution of spectral line intensities recorded is employed in a linearised form which reads

$$ln\left(\frac{I_{ij}}{A_{ij}g_i\nu_{ij}}\right) = -\frac{1}{k_BT}E_i + ln\left(\frac{FN_S\ \ h}{Q_S(T)4\pi}\right). \tag{1}$$

Then, we can rewrite Eq. (1) in a linear form; $Y = mX + q$ with the identifications

$$Y = ln\left(\frac{I_{ij}}{A_{ij}g_i\nu_{ij}}\right);\quad X = E_i;\quad q = ln\left(\frac{N_S\ \ Fh}{Q_S(T)4\pi}\right). \tag{2}$$

The slope of the line, m, gives the plasma temperature as $T = -\frac{1}{k_Bm}$. Basically, Boltzmann plot [1] graphing Y versus X summarises the distribution of energy level populations of a species when LTE prevails with an excitation temperature. Ideally, a single temperature applies to all plasma species and approaches the real thermodynamic temperature of the warm plasma. As expected, the Boltzmann plots then comprise a set of parallel lines[2, 3], and their relative abundances follow the proportionality

$$C_S \propto Q_S(T) exp(q). \tag{3}$$

If all plasma constituents are well-characterised, their absolute abundances follow the normalisation

$$\sum_S N_S = \frac{1}{F} \sum_S Q_S(T) exp(q) = 1, \tag{4}$$

from which the apparatus characteristics F may be obtained.

If a ratio of ionised states abundances is explicitly factored out from the Saha ionisation equation, separate Boltzmann plot diagrams of neutral and variously ionised states of may further reduce to a single Saha-Boltzmann plot with the following substitutions

$$Y = ln\left(\frac{I_{ij}^Z}{A_{ij}^Z g_i \nu_{ij}}\right) - Z ln\left(\frac{2\left(2\pi m_e k_B T_e\right)^{\frac{3}{2}}}{N_e h^3}\right); \quad X = E_i + Z\left(E_\infty^Z - \Delta E\right). \tag{5}$$

Hence, the Saha-Boltzmann diagram Eq. (5) can be expressed as a space of linear functions resembling Eq. (2) for which the fitted slope represents the electron temperature, $T_e \sim T$, and the linear coefficient still shows the concentration of neutral species. The most important advantage of this method, compared to the Boltzmann plot method, is that a fitted slope is obtained from two species, either an ion and a neutral atom or ions at different ionization stage and is therefore more accurate[4]. On the other hand, independent knowledge of the electron density N_e is necessary to calculate the temperature through the Saha-Boltzmann method[5].

The above procedure is fast and comprehensive but fails to offer precise results for more complex analytes or matrices. Since in our work we are prevented from using the spectroscopic diagnostics of Xe I and Xe III species, we employ the LIBS protocol to obtain a reasonable initial guess for the numerical optimisation described below.

Numerical Simulation

Numerical simulations shown in this work start with fitting fundamental spectral line parameters, *i.e.,* integral intensity and linewidth, onto Voigt line profile function

$$V(\lambda) = I_{ij} \int_{-\infty}^{+\infty} G(\lambda') L(\lambda - \lambda') d\lambda', \tag{6}$$

Where I_{ij} is the integral transition intensity fitted and $G(\lambda)$ and $L(\lambda)$ are normalised Gauss and Lorentz profiles, respectively, defined by

$$\begin{aligned} G(\lambda) &= \frac{1}{\sigma\sqrt{2\pi}} exp\left(\frac{-\left(\lambda-\lambda_{ij}\right)^2}{2\sigma^2}\right) \text{ and} \\ L(\lambda) &= \frac{\gamma}{2\pi\left(\lambda-\lambda_{ij}\right)^2+2\pi\gamma^2}. \end{aligned} \qquad (7)$$

With parameters σ and γ related to the linewidth by

$$\sigma = \frac{FWHM}{2\sqrt{2ln2}} \text{ and } \gamma = \frac{FWHM}{2}. \qquad (8)$$

The line broadening of well-defined lines for which $V(\lambda) \cong I_{ij}(\lambda)$ is then directly related to the electron density N_e through the electron impact parameter. Thereby, an initial guess on the electron density value $\hat{N}_e = N_e(\mathrm{FWHM})$ is obtained. Weak or heavily scattered peaks undergo a simple self-absorption correction, its procedure adopted from[6-9]. Based on earlier suggestions[10, 11],wavelength-dependent self-absorption coefficients are employed to relate experimentally observed signal I to its value I_0 hypothetically arisen in an ideally optically thin environment. Its definition then reads

$$\mathrm{SA} = \frac{I_0}{I} = \mathrm{FWHM}_0 \frac{1-exp(-\tau(\lambda)l)}{\tau(\lambda)} \qquad (9)$$

for an electron-broadened line width FWHM_0 and the optical depth $\tau(\lambda)$. The former is estimated by taking the instrumental broadening function enhanced merely by thermal and electron collision broadening (*i.e.,* excluding self-absorption). Since optical depth τ is, however, troublesome to calculate, the value of a self-absorption coefficient is instead deduced from the apparent linewidths measured (FWHM) and their increase from FWHM_0 as follows:

$$\mathrm{SA} \approx \left(\frac{\mathrm{FWHM}}{\mathrm{FWHM}_0}\right)^{\frac{1}{\vartheta}}, \qquad (10)$$

Which results from approximating the shape of both unaffected and self-absorbed spectral lines with a regular pulse. Usually, it is convenient to set $\vartheta = 2$[6-9]. Then, the hypothetical optically thin intensity values desired for further analyses are given by factoring our I_0 from Eq. (9) with SA read from Eq. (10). The corrected intensity values are drawn into Boltzmann plot diagrams and employed to get an initial guess on inidividual species' abundances $\hat{N}_S = N_S(q)$ by Eq. (3) . In our particular case, the abundances of Xe III are guessed from the Saha equation since, to the knowledge of authors, no transition probabilities thereof are available[12]. Integral intensities of observed transitions are then related to the theoretical line intensity I_{ij} as follows

$$I_{ij}(T,\hat{N}_S) = \int_{-\infty}^{+\infty} V\left(\lambda, FWHM = FWHM\left(\sigma_0,\hat{N}_e\right)\right), \qquad (11)$$

σ_0 is a fitted parameter of the Gaussian broadening Eq. (8) ascribed to the instrumental function and thermal broadening. Since both $\hat{N}_S$ and $\hat{N}_e$ has been guessed and are considered known, the only free parameter is plasma thermodynamic temperature T. The latter is optimised numerically until Eq. (11) holds for all experimentally observed transitions. Such an optimization yields an estimate on plasma temperature $\hat{T}$.

Next, a synthetic spectrum is drawn a sum of Voigt profile functions of individual peaks. The resultant plot with coordinates $[\lambda, I(\lambda)]$ can be directly compared with an experimental record[13] or used to yield improved values of the free parameters sought for. The procedure is iterated until at least a 98% correlation between the experimental record and a simulated spectrum is obtained. Such a spectrum is then considered fully analysed and both thermodynamic temperature and particle densities are taken for solved in terms of an LTE model.

Overall, this procedure overcomes the above mentioned issues arisen upon analysing complex or less common LIBS data, which exhibit corrupted or incomplete Boltzmann planes. However, it does not alter the physical principle of the solution, which is rather a long-time (*i.e.,* equilibrium) limit. At shorter timescale, plasma systems may be governed by various non-collisionally dominated processes which lead to energy dissipation, pressure-volume changes of a state and possibly a fully non-equilibrium behaviour. Qualitatively, such effects may be seen *e.g.,* in the temperature profiles discrepancy between $T(t, t \leq 500\,ns)$ and $T(t, t > 500\,ns)$ (see Fig. 5B in the main text). A thorough explanation of such phenomena is beyond the scope of the current paper and will be addressed in a separate plasma dynamics study.

Experimental

Apparatus

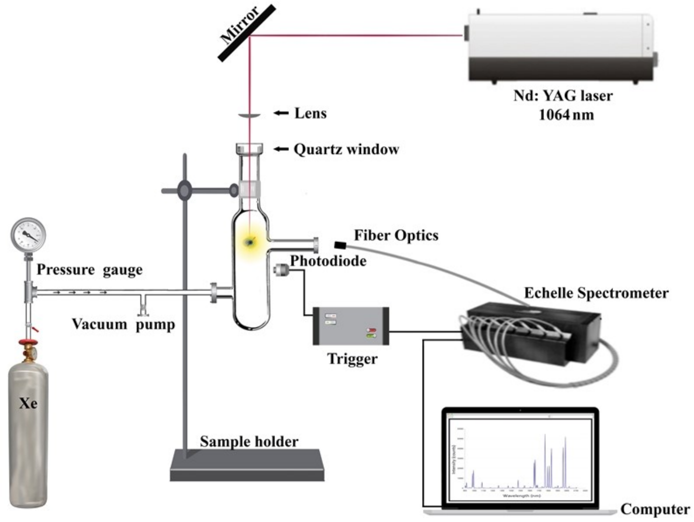

Figure S1: *Schematic diagram of LIBS experimental setup with table top Nd:YAG laser.*

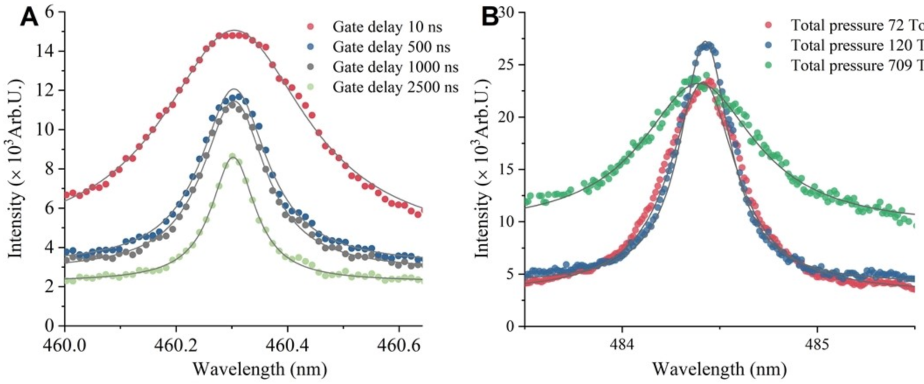

Figure S2: *(Color online) (a) Represents the Lorentzian fit for Xe II-460.304 nm at varying gate delay which is obtained using Nd:YAG laser at pressure 120 Torr. (b) Lorentzian fit for Xe II- 484.432 nm with gate delay 10 ns at various total pressures.*

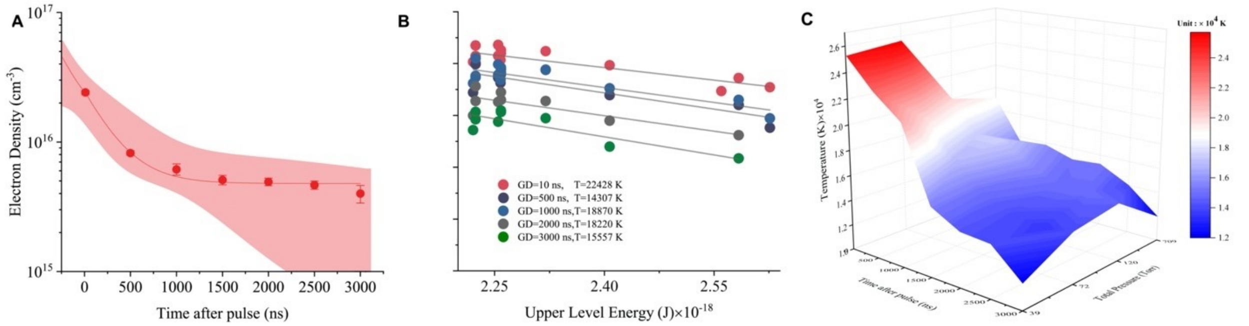

Figure S3: (*a) Represents the time evolution of the electron density for Nd:YAG experimental data for pressure 120 Torr. The solid red line shows the best fit of the data using a exponential function. The pink shadow represents the 95% confidence band in logarithmic scale for the fitted data. (b) Depicts the Boltzmann diagrams of pure Xenon measured by Nd:YAG laser at p=120 Torr for Xe II. The spectral data measurement is performed at different delay times; 10, 500, 1000, 2000, and 3000 ns. Solid gray lines show the best linear fit. (c) 3D surface profile of temperature (computed considering height at central maximum of spectral lines as the function of total pressure for different gate delay times 10, 500, 1000, 1500, 2000, 25000, and 3000 ns.*

Spectral Lines Selection and Plasma Diagnostics

During the data acquisition, all representative spectral samples were evaluated manually and fitted onto Lorentzian or Voigt profile function, as exemplified by a representative line profile fit shown in Fig. S2. The complete analysis of all spectral samples, similar to that in the main text, confirmed that mostly first ionised states (*i.e.,* Xe II) repeatedly appeared in the spectral data. For each experiment, at least five well-isolated ionic lines were selected for calculating average electron density. From Fig. S3(a), it is clear that the electron density decreases with time, since both absolute integral intensities and line widths are obviously decreased for different gate delays.

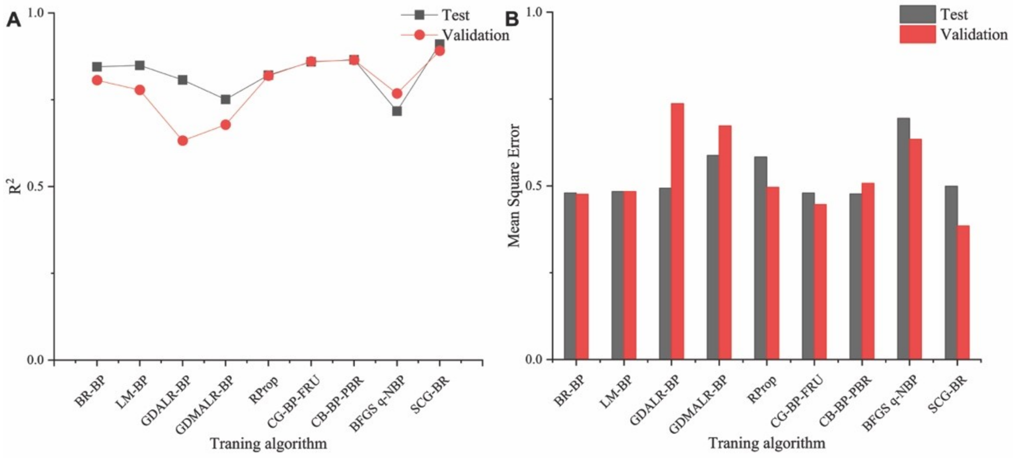

Figure S4: Optimal values of (a) correlation coefficient (linear regression) and (b) mean square error for the validation and test of temperature calculation compared among different algorithms.

Fig. S3(b) exemplifies the Boltzmann plot method adopted for calculating plasma temperatures. Despite no self-absorption corrections taken, it is clear that Xe II lines do not indeed make a scattered pattern in the single-species Boltzmann plane. Furthermore, Fig. S3(c) shows the results of estimating the plasma temperature with the time evolution of LIBS signal against different pressures of Xe gas (*i. e.*, 39, 72, 120, and 709 Torr). The experimental results found a clear support for temperature decreasing with time and slightly decreased at higher pressures. Such kind of a decreasing trend could be explained by a higher percentage of inelastic collisions which dissipate the kinetic energy of electrons. A detailed analysis of pressure-dependent data is beyond the scope of this paper, but still has a potential for further research.

Plasma Diagnostics Using ANN

Bayesian regularization back-propagation (BR-BP), Levenberg Marquardt back propagation (LM-BP), gradient descent back propagation (GD-BP), Gradient descent with adaptive learning rate backpropagation(GDALR-BP), resilient backpropagation (PRrop), Conjugate gradient backpropagation with Fletcher–Reeves(CGBPFRU), Conjugate gradient backpropagation with Powell–Beale restart (CGBPPBR), Broyden-Fletcher-Goldfarb-Shanno Quasi-Newton Backpropagation (BFGS-QNBP), and Scaled conjugate gradient back propagation (SCG-BP) as shown in Fig.S4 . As it is clear from Fig. S4 a, the CGBPFRU, CGBPPBR, and SCG-BP are in the roughly similar accuracy level. Among different training algorithms, SCG-BP algorithm showed the best performance in the test and validation steps, while the accuracy of prediction exceeded ~ 90%. The performances of all tested ANNs (with different training algorithms) are presented in the Fig.S4. Nevertheless, The SCG-BP model with the minimum validation MSE is selected for the evaluation process (See Fig. S4 b). Furthermore, the SCG-BP is the simplest and fastest one.

Plasma Diagnostics Using Numerical Simulation

State Diagrams

Abundances of the species of our interest may be depicted in the form of state diagrams plotting excited states distribution against temperature. A ratio of arbitrary adjacent ionisation states may be defined as

$$\chi(T_e,N_e) = \frac{N^{Z+1}}{N^Z} = \frac{1}{N_e}\cdot\frac{(2\pi m_e k_B T)^{\frac{3}{2}}}{h^3}\frac{2Q^{Z+1}(T)}{Q^Z(T)}exp\left(-\frac{E_\infty^Z}{k_B T}\right). \qquad (12)$$

With the right-hand side factored out from the Saha ionisation equation and partition functions taken from[12]. Our experimental results indicate that at longer observation time, electron density adopts a roughly constant trend ($N_e = \tilde{N}_e$) against temperature varying within repeated measurements. However, equilibrium electron density may in a general case vary with electron temperature, as suggested by the ionisation equilibria. To overcome this issue theoretically, the function χ can be differentiated with respect to temperature to obtain

$$\chi_T = \frac{\partial}{\partial T}\{\frac{1}{N_e}\cdot\frac{(2\pi m_e k_B T)^{\frac{3}{2}}}{h^3}\frac{2Q^{Z+1}(T)}{Q^Z(T_e)}exp\left(-\frac{E_\infty^Z}{k_B T}\right) := \frac{\partial}{\partial T}\{\frac{\varphi(T)}{N_e} \qquad (13)$$

Expanding the equation using an identification $N_e = N_e(\chi)$ and an identity

$$\frac{\partial \chi}{\partial N_e}) = \frac{\partial N_e}{\partial \chi})^{-1}$$

gives

$$\chi_T = -\frac{\partial \chi}{\partial N_e})^{-1}\frac{\partial \chi}{\partial T})\frac{\varphi(T)}{N_e^2} + N_e(\chi)\varphi'(T). \tag{14}$$

The latter equation can be solved by the method of characteristics. Our experimental data then provide an initial condition

$$\chi\left(T, \tilde{N}_e\right) = \tilde{N}_e \cdot \varphi(T). \tag{15}$$

$\varphi(T)$ is obtained by substituting the optimised heavy particle number densities into the Saha equation. Particular solutions to Eq. 14 were employed to draw the state diagrams as shown in Fig. 5(c) in the main text. Such figures demonstrate the contribution of individual species to the state behaviour of our experimental systems in a clearer way then individual spectra simulations.

Newton's Law of Cooling

The Newton's Law of Cooling can be expressed as:

$$\dot{q} = C_p \rho A d \frac{dT(t)}{dt} = -KA\left(T(t) - T_{\mathrm{bulk}}\right) \tag{16}$$

Where $\dot{q}$ is the heat transfer rate, C_p and ρ are respectively the isobaric heat capacity and mass density of the plasma spark, A is the heat transfer surface projected along a diameter d, and K is the overall heat transfer coefficient. $T(t)$ is the actual plasma temperature and $T_{\mathrm{bulk}}{}^{298.15}$ K is the bulk gas temperature recorded in the laboratory. By inspecting the relatively small overall temperature difference in Fig. 5(b) (main text) and hence by ignoring the dependencies of C_p, ρ, and K on varying temperature, we can factor out the derivative as follows

$$\frac{dT}{dt} \approx -\frac{1\ \ K}{C_p \rho\, d}\left(T(0) - T_{\mathrm{bulk}}\right) = -\,\mathrm{constant}. \tag{17}$$

In our case, since $T \gg T_{\mathrm{bulk}}$, the factor $T(t) - T_{\mathrm{bulk}}$ can be approximated by a constant difference $T(0) - T_{\mathrm{bulk}}$, giving rise to a linear trend.

References

1. A. Ciucci, M. Corsi, V. Palleschi, S. Rastelli, A. Salvetti and E. Tognoni, *Applied spectroscopy*, 1999, **53**, 960-964.
2. B. Praher, V. Palleschi, R. Viskup, J. Heitz and J. Pedarnig, *Spectrochimica Acta Part B: Atomic Spectroscopy*, 2010, **65**, 671-679.
3. M. Corsi, G. Cristoforetti, V. Palleschi, A. Salvetti and E. Tognoni, *The European Physical Journal D-Atomic, Molecular, Optical and Plasma Physics*, 2001, **13**, 373-377.

4. J. A. Aguilera and C. Aragón, *Spectrochimica Acta Part B: Atomic Spectroscopy*, 2004, **59**, 1861-1876.
5. J. Aguilera and C. Aragón, *Spectrochimica Acta Part B: Atomic Spectroscopy*, 2007, **62**, 378-385.
6. A. El Sherbini, T. M. El Sherbini, H. Hegazy, G. Cristoforetti, S. Legnaioli, V. Palleschi, L. Pardini, A. Salvetti and E. Tognoni, *Spectrochimica Acta Part B: Atomic Spectroscopy*, 2005, **60**, 1573-1579.
7. F. Bredice, F. Borges, H. Sobral, M. Villagran-Muniz, H. O. Di Rocco, G. Cristoforetti, S. Legnaioli, V. Palleschi, L. Pardini and A. Salvetti, *Spectrochimica Acta Part B: Atomic Spectroscopy*, 2006, **61**, 1294-1303.
8. M. Burger, M. Skočić and S. Bukvić, *Spectrochimica Acta Part B: Atomic Spectroscopy*, 2014, **101**, 51-56.
9. L. Sun and H. Yu, *Talanta*, 2009, **79**, 388-395.
10. I. Fishman, G. Il'in and M. K. Salakhov, *Spectrochimica Acta Part B: Atomic Spectroscopy*, 1995, **50**, 947-959.
11. I. Fishman, G. Il'in and M. K. Salakhov, *Spectrochimica Acta Part B: Atomic Spectroscopy*, 1995, **50**, 1165-1178.
12. A. Kramida, Y. Ralchenko and J. Reader, *NIST Atomic Spectra Database (ver. 5.2)[Online]*, 2014.
13. J. El Haddad, L. Canioni and B. Bousquet, *Spectrochimica Acta Part B: Atomic Spectroscopy*, 2014, **101**, 171-182.

List of Symbols

Main Text	
$h = 6.626 \times 10^{-34}$ J s	Planck constant
$k_B = 1.38 \times 10^{-23}$ J K^{-1}	Boltzmann constant
$m_e = 9.109 \times 10^{-31}$ kg	electron mass
I_{ij} (Arbitrary units)	spectral line intensity
v_{ij} (s^{-1})	$i \rightarrow j$ transition frequency
A_{ij} (s^{-1})	Einstein A coefficient
E_i (J)	upper energy level
g_i	upper energy level degeneracy
F	optical collection efficiency factor
N_S (cm^{-3})	number density of species S
Q_S	partition function
T (K)	plasma temperature
T_e (K)	free electron temperature
N_e (cm^{-3})	electron density
E_∞ (J)	ionisation energy
Z (Elementary charges)	ionisation state
ΔE (J, eV in McWhirter criterion)	energy level gap
γ (nm)	Lorentzian spectral line half-width
Ω (nm)	electron impact parameter
A (nm)	ion broadening parameter

Main Text	
N_D	plasma parameter
e	ANN error function
o	net output of ANN
t	desired output of ANN
Γ	learning constant
w,W	synaptic weights
Supplementary Information	
X (J)	independent variable in (Saha-)Boltzmann plane
Y	dependent variable in (Saha-)Boltzmann plane
q	Y-intercept of (Saha-)Boltzmann plot
m (J^{-1})	slope of (Saha-)Boltzmann plot
λ (nm)	wavelength
λ' (nm)	formal convolved wavelength
λ_{ij} (nm)	spectral line centre wavelength
σ (nm)	Gaussian spectral line width parameter
σ_0 (nm)	instrumental function line width parameter
FWHM (nm)	full width at half-maximum of a spectral line
SA	self-absorption coefficient
I_0 (arbitrary units)	spectral signal hypothetically recorded in optically thin environment
I (arbitrary units)	spectral signal measured
$\tau(\lambda)$ (m^{-1})	optical depth
l (m)	optical path
FWHM_0 (nm)	(apparent) linewidth unaffected by self-absorption
ϑ	self-absorption fitting coefficient
t (ns)	observation time
χ	ratio of adjacent ionisation states abundance
φ	temperature-dependent part of $\chi(T,N_e)$
$\dot{q}$ (J s^{-1})	heat transfer rate
C_p (J K^{-1})	isobaric heat capacity
ρ (kg m^{-3})	mass density
A (m^2)	heat transfer surface
d (m)	diameter
K (J m^{-2} s^{-2} K^{-1})	overall heat transfer coefficient